Journal of Applied Geophysics 170 (2019) 103844

Contents lists available at ScienceDirect

Journal of Applied Geophysics

journal homepage: www.elsevier.com/locate/jappgeo

Geoelectrical characterization and monitoring of slopes on a rainfall-triggered landslide simulator

Azadeh Hojat [a, b, *], Diego Arosio [c], Vladislav Ivov Ivanov [b], Laura Longoni [b], Monica Papini [b], Marco Scaioni [d], Greta Tresoldi [b], Luigi Zanzi [b]

[a] Department of Mining Engineering, Shahid Bahonar University of Kerman, Kerman, 76188, Iran
[b] Dipartimento di Ingegneria Civile, Ambientale e Territoriale, Politecnico di Milano, Milan, 20133, Italy
[c] Dipartimento di Scienze Chimiche e Geologiche, Università degli Studi di Modena e Reggio Emilia, Modena, 41125, Italy
[d] Dipartimento di Architettura, Ingegneria delle Costruzioni e Ambiente Costruito, Politecnico di Milano, Milan, 20133, Italy

ARTICLE INFO

Article history:
Received 22 November 2018
Received in revised form
2 September 2019
Accepted 5 September 2019
Available online 6 September 2019

Keywords:
Time-lapse ERT monitoring
Geoelectrical characterization
Landslide simulator
Rainfall-triggered landslides
Water saturation

ABSTRACT

In this paper, we present the results of time-lapse electrical resistivity tomography (ERT) monitoring of rainfall-triggered shallow landslides reproduced on a laboratory-scale physical model. The main objective of our experiments was to monitor rainwater infiltration through landslide body in order to improve our understanding of the precursors of failure. Time-domain reflectometry (TDR) data were also acquired to obtain the volumetric water content. Knowing the porosity, water saturation was calculated from the volumetric water content and we could calibrate Archie's equation to calculate water saturation maps from inverted resistivity values. Time-lapse ERT images proved to be effective in monitoring the hydrogeological conditions of the slope as well as in detecting the development of fracture zones before collapse. We performed eight laboratory tests and the results show that the landslide body becomes unstable at zones where the water saturation exceeds 45%. It was also observed that instability could occur at the boundaries between areas with different water saturations. Our study shows that time-lapse ERT technique can be employed to monitor the hydrogeological conditions of landslide bodies and the monitoring strategy could be extended to field-scale applications in areas prone to the development of shallow landslides.

1. Introduction

Landslides are one of the most challenging geohazards worldwide and especially in Europe. They can cause fatalities and serious injuries to people as well as damage to the property. Landslides can also damage transport infrastructures (roads and railways) located downstream of the sliding area. Aside from the costs required for repair/diversion of the damaged parts, long delays occur in transportation to and from the affected areas interrupting marketing activities, educational and health opportunities, employment and social activities (Winter et al., 2016). The high socio-economic impacts of landslides have increased interest in the development of techniques for landslide monitoring and early warning before catastrophic events.

Long-term landslide monitoring systems are helpful to minimize the adverse impacts of landslides. Examples of such real-time monitoring systems are: high-precision global positioning system (GPS) units capable of detecting small movements of the slope (Reid et al., 2012); radar systems which can continuously monitor small/large areas from short/long distances (Ross, 2017); geophysical monitoring techniques such as microseismic networks, which can detect the seismic energy released by unstable slopes (Arosio et al., 2018b), and geoelectrical methods capable of monitoring the hydrogeological conditions of the landslide body (Baroň and Supper, 2013). With repeated measurements, the monitoring systems can assess time variations of the parameters responsible for landslide activation, such as soil moisture (Crawford et al., 2019) or accelerated displacements (Michlmayr et al., 2013).

In the last decades, geophysical techniques have been increasingly used to investigate the subsurface characteristics of landslide bodies. Different geophysical techniques such as geoelectrical (Dahlin et al. 2005, 2013; Lapenna et al., 2005; Godio et al., 2006; Supper et al. 2008, 2014; Chambers et al., 2009; Lundström et al., 2009; Heincke et al., 2010; Grandjean et al., 2011; Carpentier et al., 2012; Merritt et al., 2014; Gance et al., 2016; Crawford and Bryson, 2017; Whiteley et al., 2017; Arosio et al., 2018a; Crawford et al., 2018), active and/or passive seismics (Godio et al., 2006; Heincke et al., 2010; Grandjean et al., 2011; Apuani et al., 2012; Arosio et al., 2013,

* Corresponding author. Department of Mining Engineering, Shahid Bahonar University of Kerman, Kerman, 76188, Iran.
E-mail addresses: ahojat@uk.ac.ir, azadeh.hojat@polimi.it (A. Hojat).

https://doi.org/10.1016/j.jappgeo.2019.103844

2015a, b, 2017a, b, 2018b; Longoni et al., 2014; Lundberg et al., 2014; Wang et al., 2016), ground penetrating radar (GPR) (Carpentier et al., 2012; Longoni et al., 2012; Hu and Shan, 2016), and electromagnetic (Supper et al., 2008; Grandjean et al., 2011; Wang et al., 2016) methods can be used to characterize landslide bodies. According to a review of the methods for landslide investigation and monitoring based on the information collected from 86 monitored landslides in 14 European and Asian countries, ground-based geophysical investigations most often include electrical resistivity tomography (ERT), seismic refraction and seismic reflection, self-potential, and GPR methods (Baroň and Supper, 2013). Among these methods, ERT is the most suitable to monitor soil water content variations induced by rainfalls.

Rainfall is one of the most common landslide triggers (Wieczorek, 1996; Polemio and Petrucci, 2000; Crawford and Bryson, 2018). An evaluation of a publicly available global catalog of landslides with Multi-satellite Precipitation Analysis showed that the majority of landslides were related to extreme rainfall events (Kirschbaum et al., 2015). Rainfall-triggered shallow landslides may involve large volumes of soil and are highly mobile. In rainfall-triggered landslides, the slope becomes saturated due to the rapid infiltration of rainwater and failure may develop as a result of temporary rise in pore-water pressure. This is generally believed to be the mechanism for activating most shallow landslides during storms (Wieczorek, 1996). Therefore, methods capable of detecting the hydrogeological conditions of potentially unstable slopes would be helpful in monitoring rainfall-triggered landslides.

Time-lapse ERT measurements have proven to be efficient in tracking water infiltration conditions and monitoring subsurface soil moisture in different structures such as earth embankments and landslide bodies (Godio et al., 2006; Sjödahl et al., 2008; Kuras et al., 2009; Heincke et al., 2010; Chambers et al., 2014; Perrone et al., 2014; Supper et al., 2014; Arosio et al., 2017; Whiteley et al., 2017; Crawford et al., 2018; Tresoldi et al., 2018, 2019; Hojat et al., 2019a, b, c;). Recent improvements in data acquisition systems and development of inversion algorithms have resulted in an increasing interest in using ERT method for subsurface characterization of landslides (Perrone et al., 2014). However, an enhanced understanding of the triggering processes is still required to define thresholds for slope failure. To develop such a knowledge, laboratory experiments are very useful in highlighting the critical factors and in quantifying the stability governing variables. Several authors have designed and conducted experimental simulations of reduced-scale shallow landslides triggering in the laboratory (e.g., Olivares, 2009; Montrasio and Valentino, 2016). While some researchers have investigated the applicability of analytical models (e.g., Montrasio and Valentino, 2008), others have tested the application of different instrumentations such as fiber-optic sensors (Olivares, 2009; Michlmayr et al., 2017; Schenato et al., 2017) to detect early precursors such as internal slope deformations or the generation of acoustic emissions. In our research, we studied small-scale shallow landslides on a landslide simulator designed at the Applied Geology and Geophysics Laboratory of Politecnico di Milano, Lecco Campus, Italy (Scaioni et al. 2017, 2018). The shallow landslide simulation allows the integration of geology, photogrammetry, image processing and geophysics with the aim of obtaining an exhaustive assessment of failure triggering processes. In this work, we focus on time-lapse ERT measurements to monitor the infiltration of rainfall water and to detect development of unstable zones.

2. Methodology

2.1. Equipment

The landslide simulator used in this research is a Plexiglass flume mounted on a steel frame with base dimensions of 2 m × 0.8 m. To ensure a realistic friction at the interface between the soil and the base of the frame, a geosynthetic layer was fixed at the base of the flume. A hydraulic jack attached to the bottom of the frame makes it possible to increase the inclination of the base up to 45°. Six sprinklers are fixed on the top of the frame and are used to simulate artificial rainfalls. Fig. 1a illustrates the landslide simulator and its components.

In all experiments, two GoPro Hero4 Session cameras were installed on the top frame of the landslide simulator (Fig. 1b) above the crown and toe of the slope. Images recorded by these cameras provide a continuous monitoring of the slope surface.

A time-domain reflectometry (TDR) probe (Fig. 1c) was used to collect volumetric water content data. The TDR sends a pulsed electromagnetic signal that travels along the wave guide and is reflected back at the end of the wave guide. TDR measures the dielectric constant of the soil in contact with the probe and since water is the major factor which alters the dielectric constant of soil, TDR is a tool for measuring the soil water content (Topp et al., 1984; Menziani et al., 1996). TDR datasets were used to relate resistivity values to soil water content values. In section 3.2, we discuss how we used TDR data to obtain water saturation images from resistivity sections.

To perform time-lapse ERT measurements at the laboratory scale, we prepared two 24-channel mini cables to be compatible with the IRIS Syscal Pro instrument. Cables were connected to 48 stainless steel 0.02m-long mini electrodes and were tested in a test site before landslide simulation experiments (Fig. 1d). A comparison of some common arrays was also performed to select a proper array for laboratory measurements. Due to the space limitations of the landslide simulator for electrode configurations that use remote electrodes, only Wenner, Schlumberger and dipole-dipole configurations were compared at the test site. After obtaining similar results, Wenner array was preferred to ensure a good signal-to-noise ratio (Dahlin and Zhou, 2004; Cubbage et al., 2017). Wenner array would also be a suitable configuration for real slopes, especially in remote and inaccessible areas, because minimum current injection would be an advantage for permanent monitoring systems that use solar panels as the energy supply.

2.2. Laboratory experiments

We performed eight laboratory experiments to simulate rainfall-triggered shallow landslides. Each experiment ended with the collapse of the slope and we never used again a previous model or the material remaining from a previous test. The slope material used in all experiments was uniform fine sand with $d_{50} = 0.35$ mm. To construct the landslide body, a 0.15m-thick layer of sand was laid on the landslide simulator. Such a thickness satisfies the condition $h/l < 0.1$, where h and l are the slope thickness and length, respectively. This condition is usually required to adopt the hypothesis of infinite slope used in slope stability analysis (Milledge et al., 2012). The compaction of the soil was controlled by a fixed relationship between the volume occupied by the landslide body and the mass of the constituting material. Porosity of the landslide body for various experiments ranged between 52%-54%. We used different initial volumetric water contents in order to investigate a variety of cases from very dry soil to rather wet soil. The initial volumetric water content was measured with the TDR probe after preparing the landslide body for each test. Different rainfall patterns were simulated during each experiment. Some experiments simulated rainfall events consisting of a constant rainfall followed by a pause and another constant rainfall. In other cases, a constant or gradually increasing rainfall event was simulated. Rainfall intensity was estimated considering the known sprinkler discharge and the area affected by the spray cones, where a uniform rainfall distribution was assumed. Table 1 summarizes experiment setups for different tests.

Fig. 1. a) Landslide simulator used for simulating rainfall-triggered shallow landslides. b) A closer view of the top frame of the landslide simulator with two GoPro Hero4 Session cameras installed. c) TDR probe used for measuring the volumetric water content. d) Preparation and testing of two 24-channel mini cables connected to mini electrodes.

The Wenner array with unit electrode spacing a = 0.03 m was used for ERT measurements. In the first experiment, the electrodes were placed in two parallel lines (24-electrodes each) perpendicular to the slope dip direction (test no. 1 in Table 1) and, after the failure of the very bottom section of the slope, the landslide body collapsed along the lower ERT line. Thanks to this experiment, we realized that a spread perpendicular to the slope dip direction could disturb the tests by generating a discontinuity that might evolve into a fracture. Moreover, such a layout would be less effective in detecting weak zones and in monitoring rapid resistivity changes and failures generally occurring along the slope dip direction. Therefore, we decided to deploy the ERT spread parallel to the slope dip direction in all the other tests to monitor resistivity changes from the crown to the toe. Using 48 electrodes with the electrode spacing of a = 0.03 m, the ERT profile was 1.41 m, long enough to adequately map the landslide body parallel to the slope dip direction (Fig. 2a). Mini cables and electrodes were buried at 0.01 m or 0.02 m depth to prevent preferential infiltration pathways at the locations of electrodes. In the first four experiments, a resistivity pseudosection was measured every 9.5min. The time interval between each measurement was later reduced to 3.5min, using the high-speed option of the IRIS Syscal Pro resistivity-meter. This helps to obtain a more continuous record of resistivity changes with the rainfall and before any failures, and thus, to better monitor the variations of water saturation and to detect possible thresholds for slope failure. TDR probe was also used in all experiments, buried at a known depth and location. Fig. 2b shows an example of resistivity and TDR measurements during a simulated rainfall event. Failure of the lower section of the slope results in large displacements so that the electrodes at that location lose the contact with the soil. As a consequence, resistivity measurements were continued using only the 24 upslope electrodes still in contact with the soil with a high-speed rate of one measurement every 1.5min.

2.3. Data processing

2.3.1. Artefacts from laboratory simulator

After preparing the slope and before activating the rain sprinklers, an initial measurement of the soil resistivity (hereafter named T_0) was carried out for all the experiments. Considering the

Table 1
Experiment setups for landslide simulation tests. The slope material was homogeneous sand.

Test No.	ERT layout	Initial volumetric water content (%)	Slope angle (degrees)	Rainfall intensity (mm/h)
1	Perpendicular to the slope dip direction 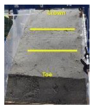	12.5	33	48.5: for the first 10min 0: during t = 10-20min 81: from t = 20 min until the end of the test
2	Parallel to the slope dip direction 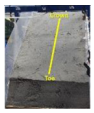	11.5	40	48.5: for the first 10min 0: during t = 10-20min 81: from t = 20 min until the end of the test
3	Parallel to the slope dip direction	4.0	40	54: for the first 10min 0: during t = 10-20min 94.5: from t = 20 min until the end of the test
4	Parallel to the slope dip direction	10.0	40	48.5: continuous during the test
5	Parallel to the slope dip direction	9.0	35	48.5: for the first 10min 0: during t = 10-20min 81: from t = 20 min until the end of the test
6	Parallel to the slope dip direction	13.3	35	Gradual increase from 72.8 to 98
7	Parallel to the slope dip direction	13.7	40	77.2: for the first 10min 0: during t = 10-20min 83.6: from t = 20 min until the end of the test
8	Parallel to the slope dip direction	5.0	35	124: continuous during the test

typical values of low-saturated sands, the initial resistivity was expected to be in the range of 400-600 Ωm depending on the soil properties such as porosity, degree of compaction, and initial volumetric water content.

All measured apparent resistivity pseudosections showed that apparent resistivity values of deeper layers were anomalously high. This is because the base of the landslide simulator is covered by Plexiglass, which is an electrically resistive material. Fig. 3a shows an apparent resistivity pseudosection measured at T_0 for an experiment in which the average resistivity of the soil was 550 Ωm. This value is obtained by averaging the measurements with the shortest electrode spacings in the middle of the profile. The increasing gradient is clearly seen in the measured pseudosection. The sharp gradient in the measured pseudosection is not related to resistivity changes within the soil layer, rather it is due to the resistive base. To validate this hypothesis, a synthetic two-layer model was constructed in RES2DMOD (Loke, 2016). The resistivity of the first layer was set 550 Ωm. This homogeneous layer was defined over a resistive layer at the depth of 0.14 m. The calculated apparent resistivity pseudosection of this synthetic model is shown in Fig. 3b. The comparison between Fig. 3a and b shows that the calculated apparent resistivity pseudosection is in good agreement with the measured one. Since the side walls of the landslide simulator are also made from plexiglass (see Fig. 1a), we explored how these resistive walls may affect the measurements. A 3D synthetic model was constructed in RES3DMODx64 (Loke, 2014) with a homogeneous layer having the resistivity of 550 Ωm confined by two resistive side walls 0.8 m apart, representing the

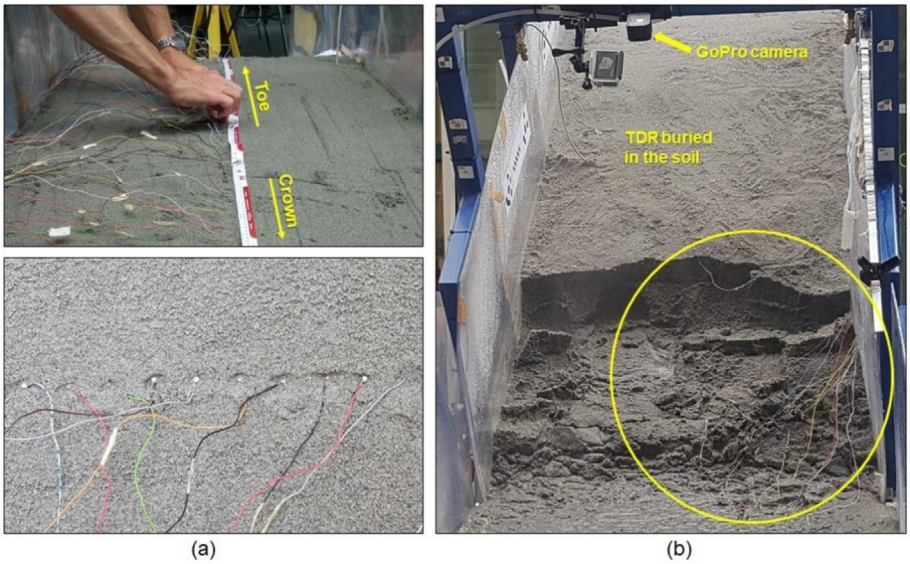

Fig. 2. a) Deployment of the mini electrodes along an ERT profile. b) An example of time-lapse ERT and TDR measurements. TDR was buried horizontally in the slope body. The yellow circle shows the downslope electrodes exposed after the failure.

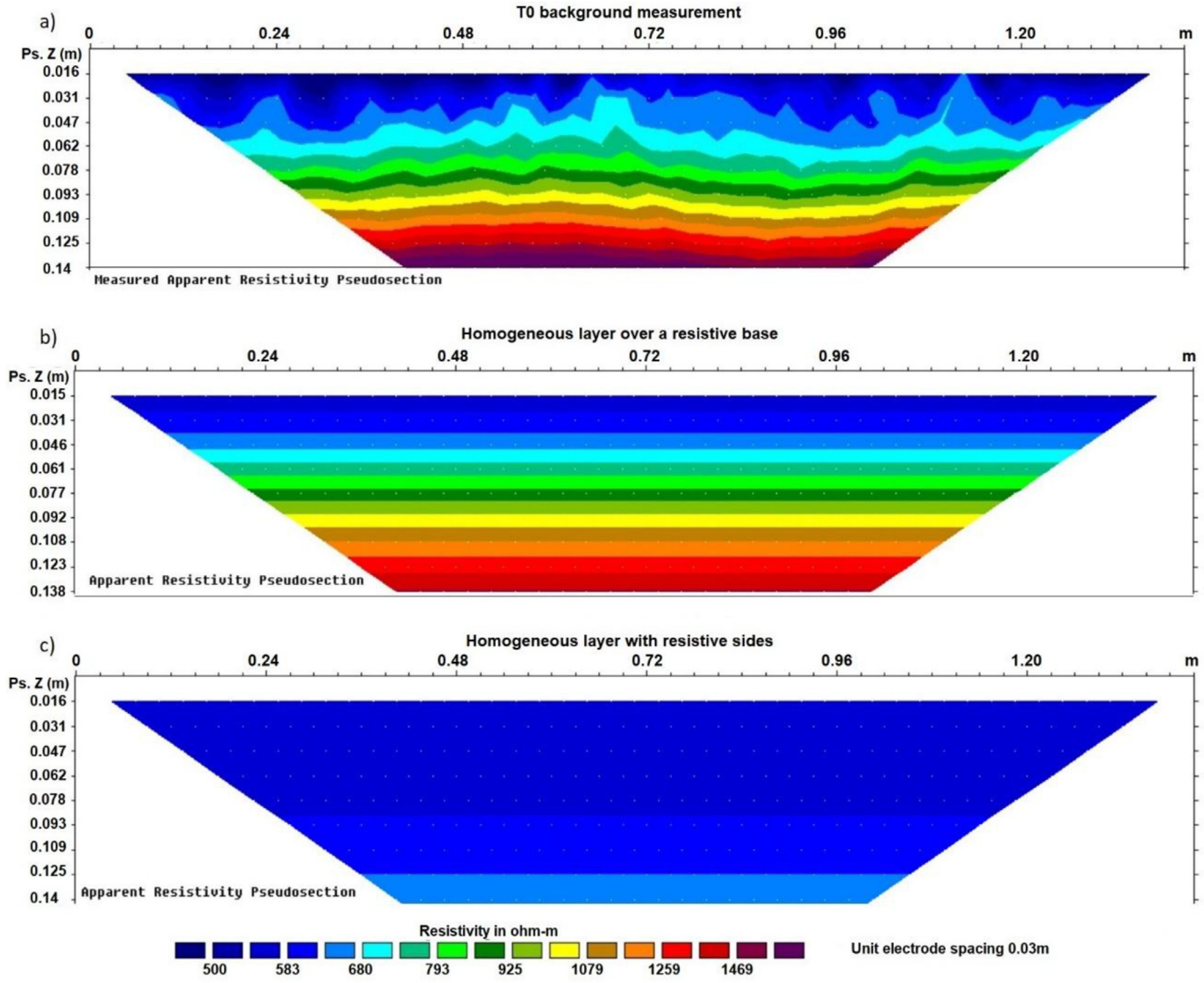

Fig. 3. a) Measured apparent resistivity pseudosection obtained at T_0 for a homogeneous slope with resistivity of about 550 Ωm. b) Calculated apparent resistivity pseudosection for a homogeneous layer of 550 Ωm over a resistive layer, modelled in RES2DMOD (Loke, 2016). c) Calculated apparent resistivity pseudosection for a 550 Ωm homogeneous layer with resistive side walls; ERT profile mid-way from the side walls modelled in RES3DMODx64 (Loke, 2014).

Plexiglass side walls of the landslide simulator. The calculated apparent resistivity pseudosection of this model along the profile located midway from the side walls is shown in Fig. 3c. It is seen that most of the calculated values are similar to the defined resistivity for the soil layer. Therefore, a comparison of the images in Fig. 3 shows that the main anomalous increase of measured resistivity values with depth arises from the effect of the resistive base of the landslide simulator. To account for sharp changes of resistivity values across this boundary and to obtain accurate resistivity images of the soil layer after inverting the data, the base of the landslide simulator was introduced as a resistive sharp boundary in all inversions of the data performed in RES2DINVx64 (Loke, 2018). This will provide meaningful inverted images to be reasonably interpreted, as we will see later in Figs. 5–7.

2.3.2. Buried electrodes

In ERT measurements, the electrodes are generally located on the surface and the current flows in the lower half space. Since the electrodes are buried in our experiments, the effect of buried electrodes needs to be corrected because the current also flows in the soil layer above the electrodes. The effect of buried electrodes can be quantified by the analogy between the electrical situation and optics (Telford et al., 1990). Fig. 4a shows the electrical image for a current electrode (I) buried at the depth h. The potential measured at any point P is partly due to the current electrode (I) and partly due to its image in the second medium. This well-known concept was used to calculate the ratio of apparent resistivity measured by buried electrodes to resistivity of the half space. We calculated this ratio considering the Wenner array with unit electrode spacing a = 0.03 m and the electrodes buried at 0.01 m depth, and we observed that, when the electrodes are buried, the measured apparent resistivity values are smaller than the real resistivity of the soil, especially for the smallest electrode spacings (Fig. 4b).

2.3.3. Inversion of datasets

All the datasets were further filtered for negative resistance values, bad quality factors (standard deviation larger than 2%), and extremely low current. The datasets were then inverted using RES2DINVx64 with the robust option (Loke, 2018), which is in

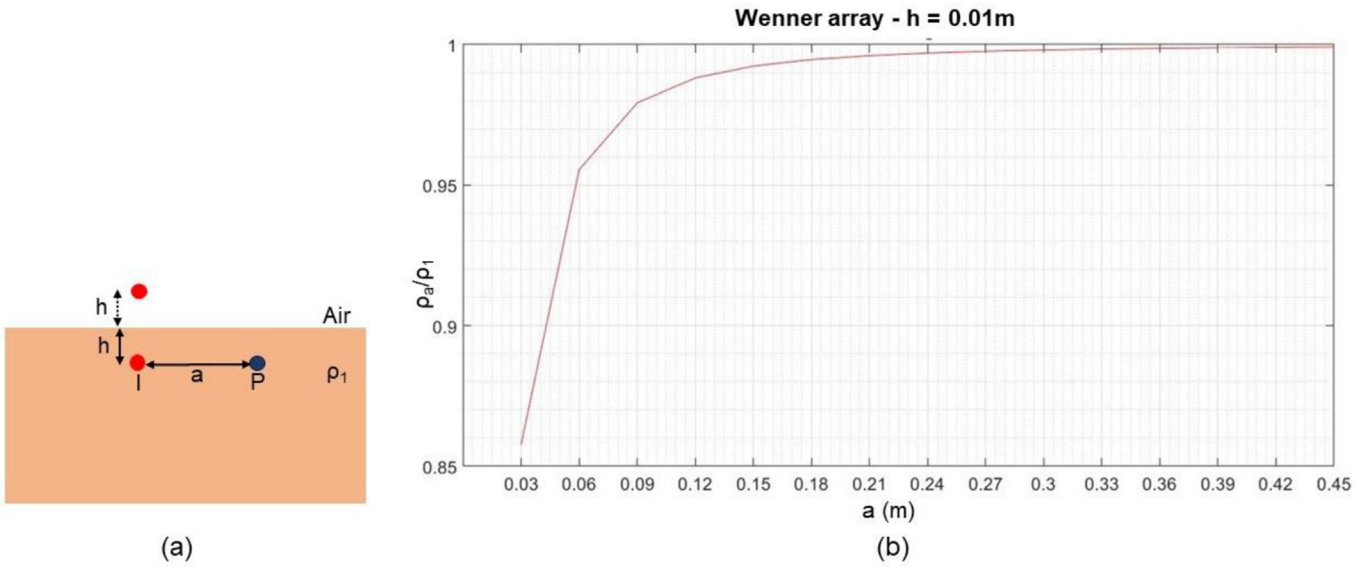

Fig. 4. a) Electrical image concept for a current electrode (I) buried at the depth h. b) The ratio of apparent resistivity measured by buried electrodes to resistivity of a homogenous layer for the Wenner array with unit electrode spacing of a = 0.03 m and the electrodes buried at 0.01 m depth.

principle superior to the smoothness-constrained least-squares inversion (Loke et al., 2003; Dahlin and Zhou, 2004).

3. Results and discussion

3.1. Detection of failure zones

Fig. 5 illustrates an example of inverted resistivity sections for an experiment (test no. 5 in Table 1) where ERT profiles were measured with the high-speed option to minimize the time required for data acquisition. Acquisition of each pseudosection with 48 electrodes took about 3.5min. The sprinklers simulating rainfall were activated at the beginning of the experiment for 10 min. Rainfall was then stopped for 10 min and then re-activated until the end of the experiment. Time-lapse resistivity images show resistivity variations of the soil layer above the resistive base of the landslide simulator. The resistivity image at T_0, theoretically expected to be a homogeneous body with uniform distribution of moisture, shows how non-uniform compaction of the soil in different areas results in changes in the resistivity values of the soil. The resistivity image at t = 11min is measured after the first rainfall event and as expected, it shows the decrease of resistivity values due to infiltration of the rainwater. Distribution of water saturation, and thus of resistivity values, is not homogenous within the landslide body because of the irregular soil compaction and preferential flow paths for the water. Moreover, the rainfall intensity was not homogenous over the slope surface due to the limited number of sprinklers. Measurements of t = 19min started 9min after the end of the initial rainfall event, and just 1min before the sprinklers were re-activated. Therefore, since each ERT profile was measured in about 3.5min and the measurement sequence progressively moves from left to right of the sections, lower resistivity values were recorded on the right side of this profile, which was measured when the landslide body was experiencing the second rainfall. Since the landslide body was stable until t = 36min (Fig. 6), we show just a resistivity image every 10.5min from T_0 until t = 30min in Fig. 5 to display the infiltration of rainfall water. Then, to explore the possibility of detecting weak zones that began to develop after t = 35min, all the three measured ERT sections from t = 30min until t = 37min are shown. The resistivity image at t = 30min illustrates again that after activating the rain sprinklers and due to the infiltration of rainwater, measured apparent resistivities continue to decrease considerably. The landslide body has higher saturation values (lower resistivity values) during this second rainfall. The resistivity image at t = 34min shows a highly saturated zone at the toe of the slope. In the middle part of this section, we can observe a less saturated surface zone located over a more saturated mass at depth. The resistivity image at t = 37min was the last profile measured using all 48 electrodes. It shows the increase in resistivity values at 0.09–0.12 m from the toe on the surface, within the highly saturated part of the landslide body. This abrupt change is due to the formation of a fracture that resulted in the failure of the lowermost section of the slope (Fig. 6). This image also shows the initial time of formation of another fracture that develops at the distance of 0.73 m on the surface. At t = 40min, the downslope electrodes lost their contact with the soil due to the collapse of the lower part of the landslide body and measurements with only the 24 upslope electrodes could be performed afterwards.

Fig. 6 shows the pictures of the slope taken at times t = 35min, t = 36min, t = 37min, and t = 38min for the test shown in Fig. 5. The correlation can be recognized between the high resistivity zones at times t = 37min and t = 39min in ERT measurements and the corresponding F3 and F4 fractures observed on the pictures. Unfortunately, we could not continue to monitor resistivity changes related to the development of F4 unstable zone because this fracture was located approximately in the middle of the profile and after the electrodes in the lower section of the slope were exposed, data coverage was not sufficient in this area. The pictures taken with GoPro cameras show that the landslide body started to fail at the location of F4 at t = 46min, therefore, resistivity images could detect this weak zone well in advance. By correlating the resistivity images at t = 30min, t = 34min, and t = 37min in Fig. 5 with the positions of fractures F3 and F4, it can be observed that F3 occurs within a highly saturated zone while F4 develops in a less saturated zone in correspondence of a resistivity change. More in detail, F4 is developing in a less saturated surface zone that is located over a more saturated mass at depth. Thus, this experiment suggests two possible indicators of unstable zones that might evolve into new fractures: 1) areas where water saturation exceeds a threshold level, and 2) large gradients of saturation levels within the slope. To quantify these indicators, we need to transform resistivity measurements into water saturation images, as will be discussed in section 3.2. At this stage we can anticipate that this transformation will result in a saturation warning level of about 45%. Of course the warning level is

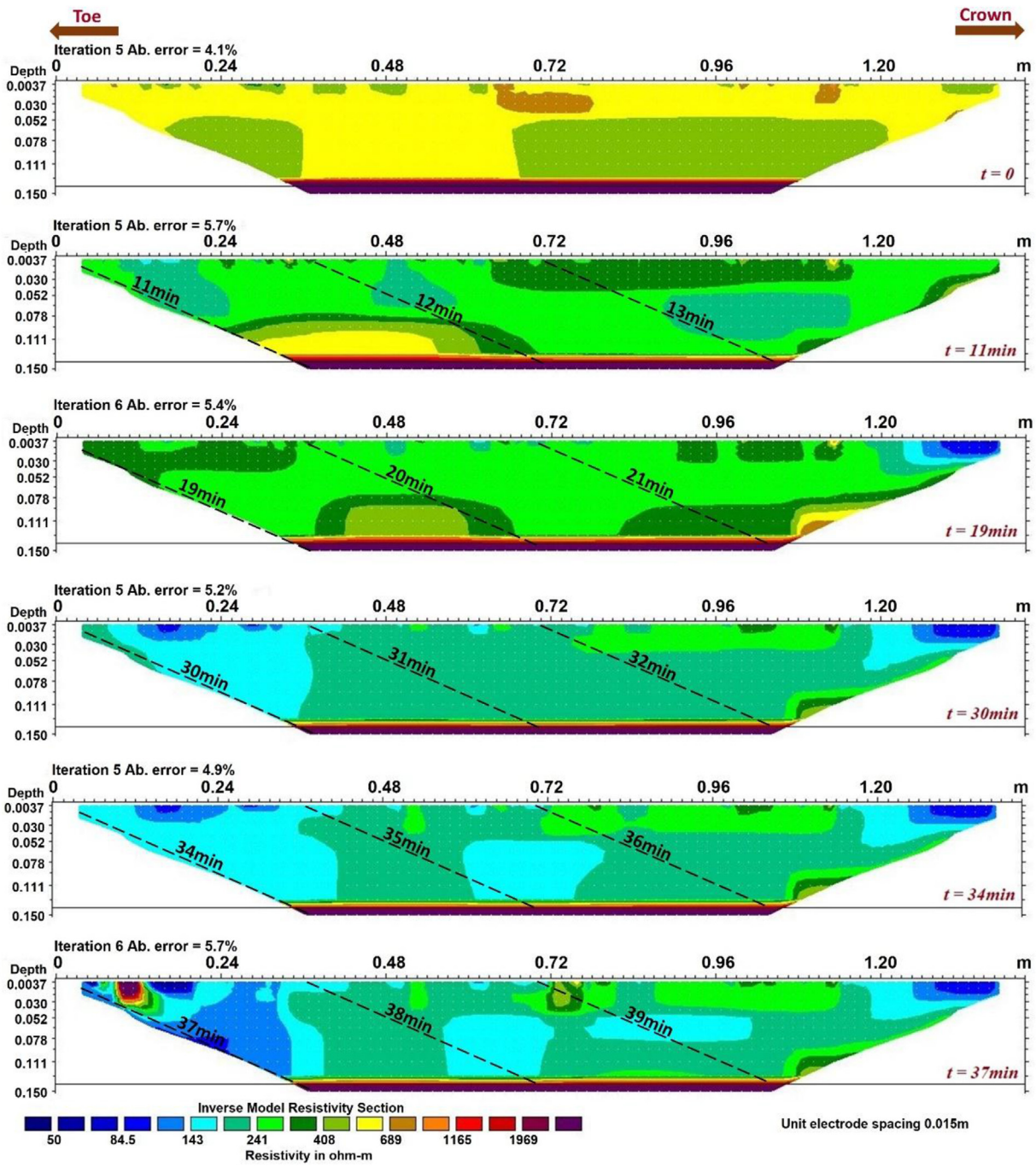

Fig. 5. An example of inverted resistivity sections (test no. 5 in Table 1). The diagonal dashed lines on the resistivity sections show the approximate time of measurements (increasing from left to right). At t = 37min, a fracture began to develop at the distance of 0.09–0.12 m from the toe on the surface, which later resulted in the failure of the lowermost part of the slope at t = 40min.

also dependent on the landslide material (sand for these experiments) and on the slope angle (about 35° for this example).

Fig. 7 illustrates the results of another experiment (test no. 4 in Table 1) in which high resistivity zones consecutively appeared one after another (Fig. 7a) in correspondence of the development of different fracture zones (Fig. 7b). This is an example of experiments where each ERT measurement took 9.5min to be completed. The pictures in Fig. 7b show a fracture (named F1) starting to develop 28min after the beginning of the experiment at the distance of x = 1.34 m from the toe of the slope on the surface. Data acquisition of the resistivity section at t = 21min continued for 9.5min. Therefore, this resistivity section could record the high resistivity zone corresponding to fracture F1. The next resistivity section was measured from t = 31min and recorded two other high resistivity zones which correspond to the development of two new fractures (F2 and F3) at x = 0.9 m and x = 0.15 m from the toe of the slope. Similarly, the times and locations of F2 and F3 observed on GoPro pictures are well correlated with the detected high resistivity zones. As for F4 in Fig. 6, weak zones in this experiment were mainly located at the borders between areas with different water saturations. Abrupt high resistivity zones corresponding to the formation of fractures were observed in most of the experiments

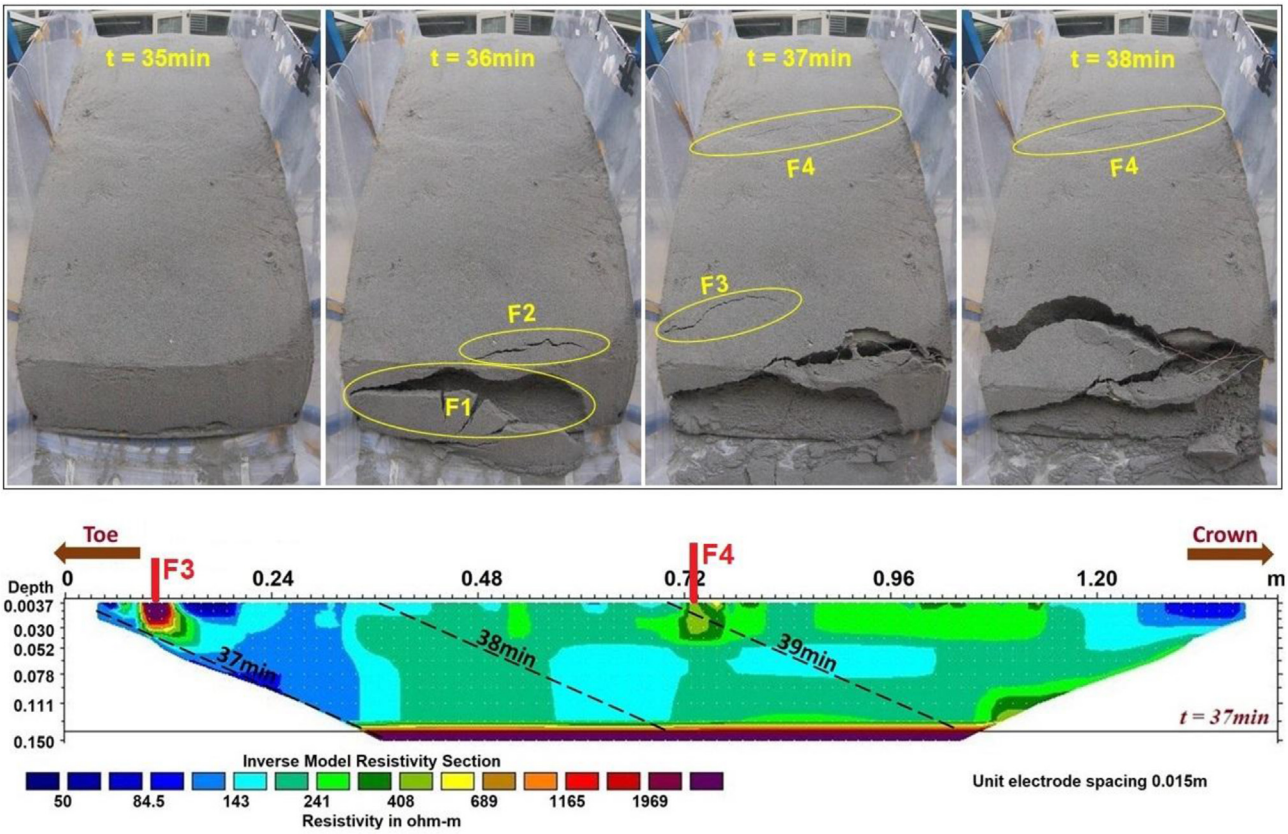

Fig. 6. Correlation between the times and the distances of the high resistivity zones recorded at t = 37min (Fig. 5) with fractures F3 and F4 observed on the pictures. Fractures F1 and F2, developed at t = 36min, are located on the landslide toe outside the ERT profile.

and were well correlated with the times and locations of the fractures observed on GoPro pictures.

After the collapse of the lower section of the landslide body, which resulted in the detachment of the downslope electrodes in all the experiments (Fig. 2b), resistivity measurements were continued using only the 24 upslope electrodes that remained in contact with the soil. In a couple of experiments, the resistivity values did not change considerably and new failures did not occur for about 30min, so the experiment was stopped. In other experiments, additional high resistivity zones corresponding to the development of new fractures were recorded and thus, resistivity measurements were continued until the upslope section also collapsed.

Fig. 8 shows an example of new fractures occurring in the top part of the profile and their detection on resistivity sections. This is an example of an experiment (test no. 6 in Table 1) with high-speed acquisitions where each measurement with 24 electrodes took about 1.5min to be completed. The resistivity section at t = 35min clearly shows that the development of fracture F1 is promptly detected. A comparison of the three resistivity sections at the distance of about x = 0.9 m along the surface (red arrow in Fig. 8a) reveals the potential of ERT in predicting unstable zones. A high resistivity zone starts to develop at the surface at the border of a localized high-saturation part at about t = 33min (see section at t = 35 and t = 37min in Fig. 8a). This sudden increase of resistivity corresponds to the fast formation of a new and significant failure (F2) occurring in a couple of minutes. Air is getting into the fracture and the resistivity is thus increased. The rapid evolution of F2 is clearly recorded in the pictures shown in Fig. 8b. It is interesting to note that F2 is not visible on the picture at t = 35min, while the resistivity values registered at this time are already increasing with respect to previous measurements.

3.2. Water saturation vs. resistivity

After inversion of all resistivity data, TDR data were used to establish the petrophysical relationship between water saturation and resistivity for the material used in our experiments. Archie's law (Archie, 1942) is valid for clay-free formations with highly resistive mineral grains and thus, it is applicable to the sand material used in our experiments:

$$\rho = FS_w^{-n}\rho_w \tag{1}$$

where ρ is the resistivity of the material, F is the formation resistivity factor, S_w is the water saturation, and ρ_w is the resistivity of the water in pores. n is the saturation exponent varying in the range $1.2 \le n \le 2.2$ and is determined empirically. The formation resistivity factor is related to porosity (φ) by the formula:

$$F = a\varphi^{-m} \tag{2}$$

where $0.5 \le a \le 2.5$ and $1.3 \le m \le 2.8$.

The volumetric water content, θ, was monitored using TDR data. Following the definitions of the water saturation and volumetric water content, we have:

$$\theta = \frac{V_w}{V_t} \tag{3}$$

$$S_w = \frac{V_w}{V_{pore}} = \frac{\theta}{\varphi} \tag{4}$$

where V_w, V_{pore} and V_t are the volumes of water, pores, and the total material, respectively.

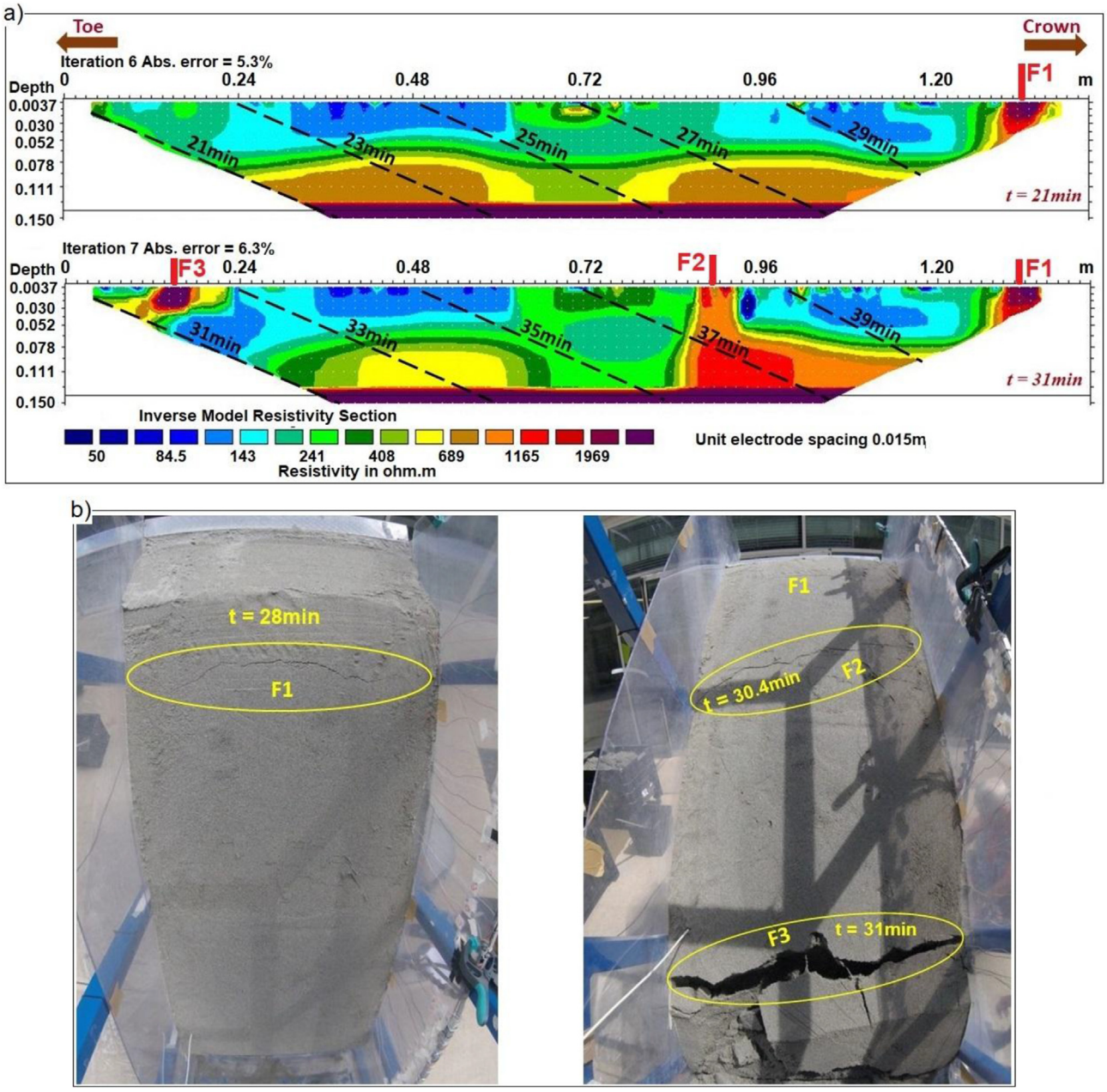

Fig. 7. a) Two successive resistivity sections (test no. 4 in Table 1) showing high resistivity zones recorded at distances x = 1.34 m (F1), x = 0.9 m (F2), and x = 0.15 m (F3) from the toe of the slope on the surface. The diagonal dashed lines on the resistivity sections show the approximate time of measurements (increasing from left to right). b) Times and locations of the fractures recorded by GoPro cameras.

Using the volumetric water content values and inverted values of resistivity at the location of TDR measurements, we calculated the coefficients of equation (1) assuming a porosity of the soil equal to 54%. Porosity of different landslide simulations was actually slightly varying around this value.

As a first trial, we assumed a = 1 and m = 2 to obtain F from equation (2). Knowing the volumetric water content at T_0 from TDR, we calculated S_w from equation (4). We know that the resistivity of water used in the rain sprinklers was 27 Ωm. Assuming n = 2, the calculated resistivity from equation (1) was higher than the inverted resistivity value at T_0. Therefore, the coefficients were reduced to fit the calculated and inverted resistivity values. Values of a = 0.5, m = 1.3 and n = 1.7 were found to give the best matching results. To validate the calibrated coefficients, the resistivity values were calculated from TDR data at different times. The calculated resistivity values at each time were compared with the inverted resistivity values at the location of TDR at the same time. We compared the calculated resistivity values at each time with the inverted resistivity values at the location of TDR at the same time and we found a good agreement. As a result, we developed the following equation to obtain the water saturation of the landslide body from inverted resistivity data:

$$S_w = \left(\frac{29.7}{\rho}\right)^{0.59} \quad (5)$$

Fig. 9 shows water saturation versus resistivity plotted based on Eq. (5). Resistivity of the soil always decreases as water saturation increases, but, as common in soils of resistive grains such as clean sands, the relation between water saturation and resistivity is not

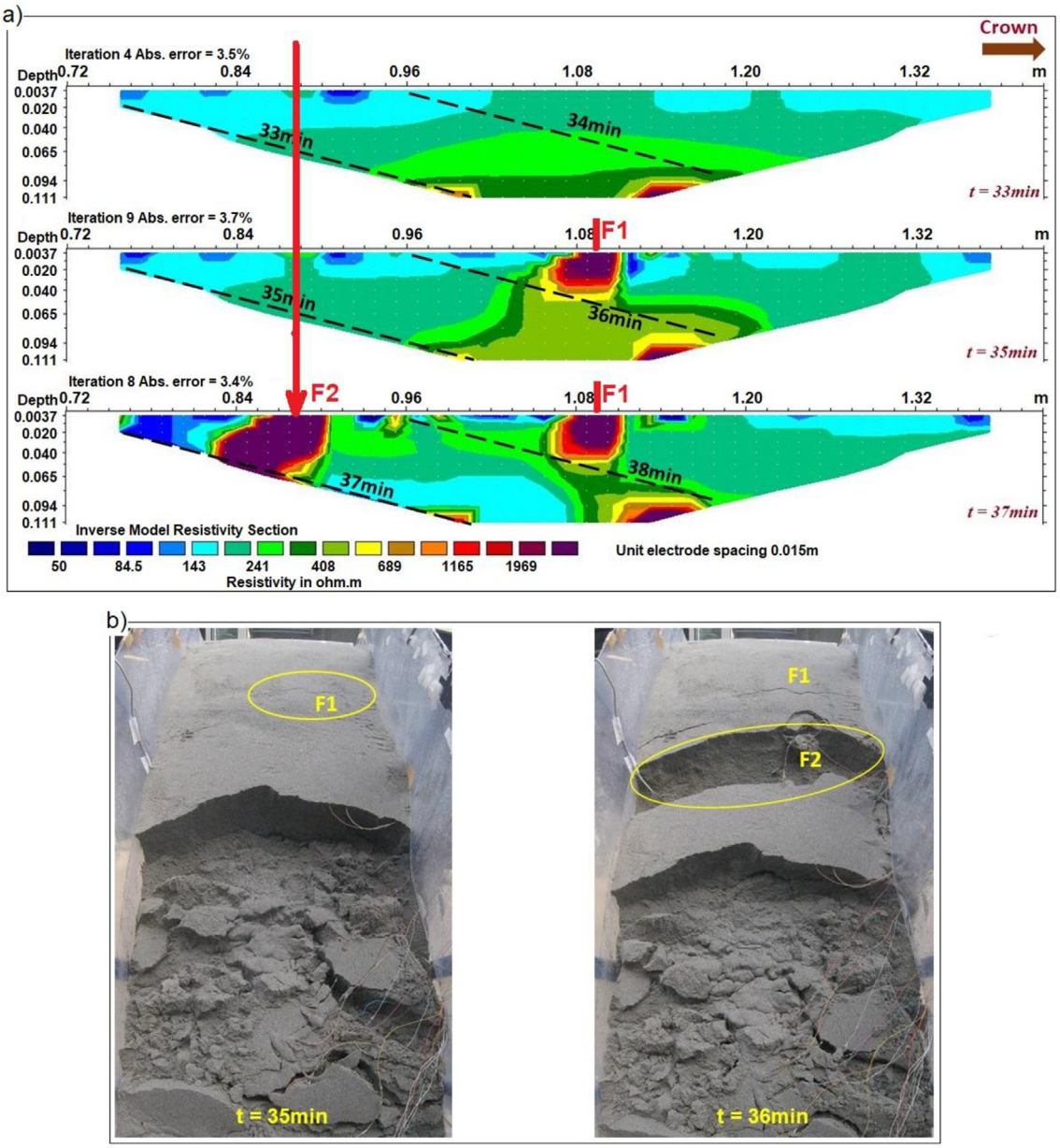

Fig. 8. An example of new fractures developed after the collapse of the lower part of the slope (test no. 6 in Table 1). a) New fractures (F1 and F2) are detected in ERT images obtained from measurements with the remaining 24 electrodes. The diagonal dashed lines on the resistivity sections show the approximate time of measurements (increasing from left to right). The red arrow shows the fast development of fracture F2. b) Times and locations of the fractures recorded by GoPro cameras.

linear (Mooney, 1980). Moving from an almost dry soil to water saturations of about 30-40%, the resistivity values decrease considerably due to the role of water in conduction (the water was not very resistive in our experiments). Further increases in water saturation beyond about 40% still reduces the resistivity values, but more gently.

Having developed the petrophysical relation between resistivity values and water saturation of the landslide body (Eq. (5)), all inverted resistivity sections were converted to water saturation images. Fig. 10 shows time-lapse water saturation images obtained from the resistivity sections discussed in Fig. 5. In this experiment, the landslide body experienced a failure at t = 37 min at the location indicated by the black arrow in Fig. 10. The unstable zone developed at the boundary of a wet area where S_w exceeds 45%.

Time-lapse water saturation images of all the experiments were compared with the times and locations of failures. In 80% of the

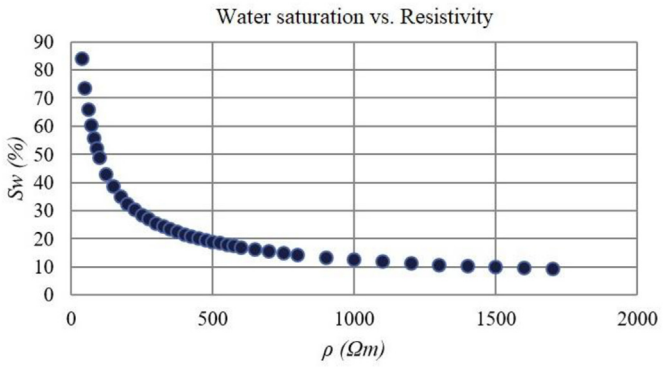

Fig. 9. Graph of soil water saturation versus resistivity values based on Eq. (5), which was developed for the material used in our landslide simulation experiments.

experiments, the landslide body became unstable at the borders between zones with different water saturation or where the water saturation of the soil exceeds 45%. A careful study of the images showed that the delay from the time a fracture was recognized on the resistivity sections until the failure of the related area ranged from 1 min up to 10 min. Considering the reduced scale of the experiments as well as the simulation of extreme precipitation, the time scales observed here could imply much larger time spans if a real-scale case study is to be monitored. A deeper soil layer would naturally require more time to be saturated although upscaling is most likely not directly proportional (Iverson, 2015).

4. Conclusions

Our ERT monitoring tests of rainfall-triggered shallow landslides showed that rainfall infiltration paths through the soil were variable resulting in inhomogeneous zones of water accumulation. By comparing volumetric water content values obtained from time-

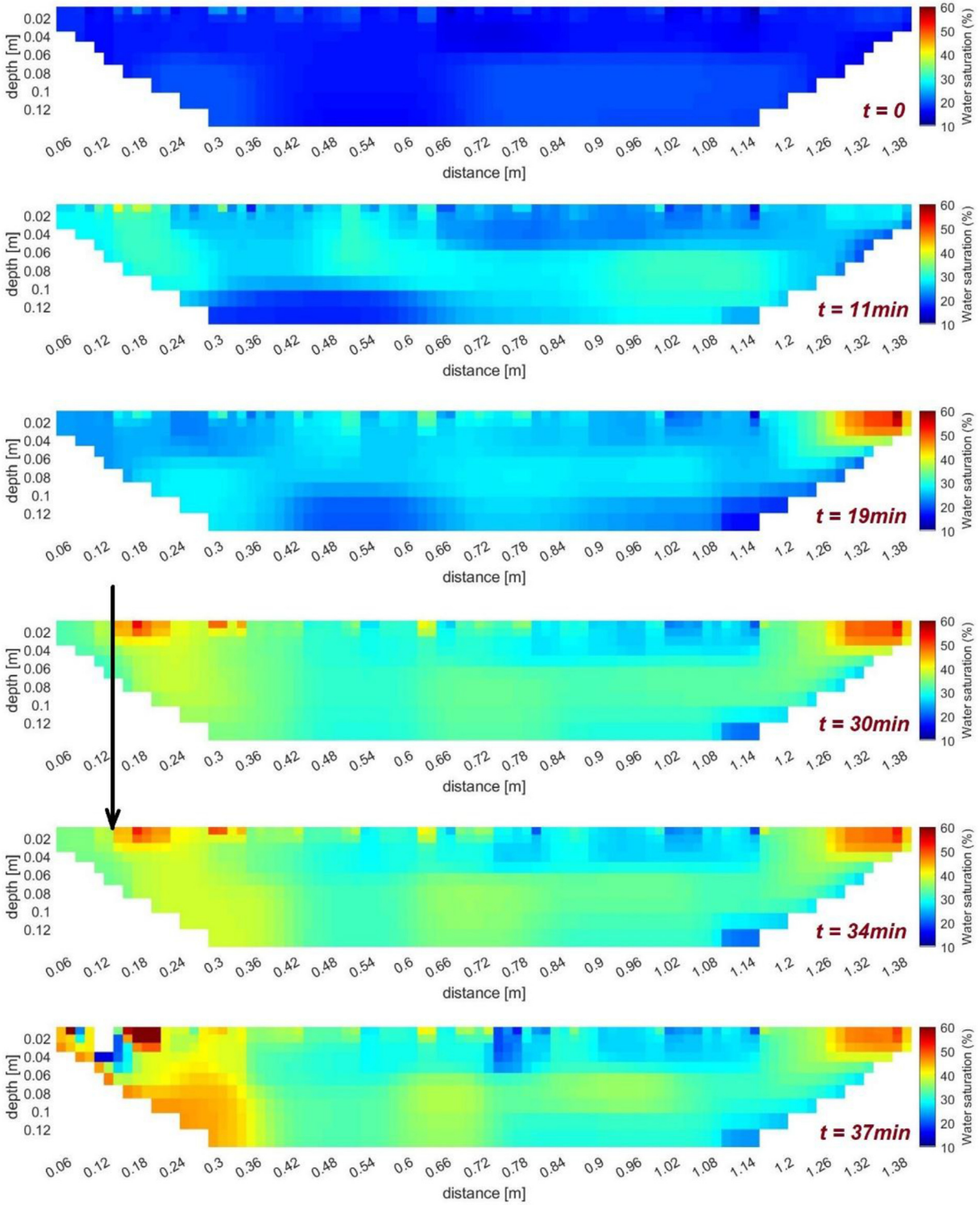

Fig. 10. Time-lapse water saturation images obtained from the inverted resistivity sections shown in Fig. 5. The black arrow shows the location of a failure occurring at t = 37min.

lapse TDR measurements with inverted resistivity values measured nearby the TDR sensor, we were able to calibrate the coefficients of Archie's law. We observed that time-lapse ERT measurements could effectively monitor time changes in water saturation within the landslide body. Fractures were found to develop at the borders between zones with different water saturation, or where the soil was highly saturated. In particular, saturations higher than 45% were found to generate slope instability. This is a threshold related to the specific material and the specific dip values selected for our experiments. Nevertheless, our results indicate that laboratory tests could be successfully used to simulate various scenarios and to estimate thresholds specifically related to a real landslide.

Time-lapse ERT images could predict development of fractures where abrupt high resistivity discontinuities were recorded. The most frequent delay from fracture formation to failure detected on GoPro images was in the order of a couple of minutes. However, our example of high-speed ERT measurements showed that development of fractures can be detected in ERT sections even before the fractures are visible on GoPro images. One of the future perspectives is to estimate more accurately the time lag from ERT fracture detection to formation of visible fractures as well as between fracture appearance and collapse and convert it from the laboratory scale to the real scale, in order to use it for implementing an early warning procedure. Our results show that geoelectrical methods can be effectively employed as parts of early warning systems for unstable slopes. However, in order to define landslide triggering thresholds based on water saturation, more experiments should be performed to correlate different governing parameters. Further experiments with different soil materials, such as clay, may help to better characterize landslide mechanisms in a more complex context.

One of the limitations of our ERT investigations was the low frequency of measurements due to the time required for each acquisition. Measurements should be rapid enough to follow the fast processes involved in the failure of rainfall-triggered landslides without any aliasing and to avoid misunderstanding of the processes and loss of valuable pieces of information. In order to make ERT technique as efficient as possible, development of high-speed ERT monitoring systems capable of operating and being programmed remotely is encouraged.

Declaration of Competing Interest

None.

Acknowledgements

We are grateful to Dr. Meng Heng Loke for his valuable comments on 2D and 3D forward modelling studies. The authors also thank the journal editor, Dr. Mark E. Everett, and two anonymous reviewers for their suggestions and thorough reviews that helped to improve the manuscript significantly.

Appendix A. Supplementary data

Supplementary data to this article can be found online at https://doi.org/10.1016/j.jappgeo.2019.103844.

Funding

This research was partially funded by Fondazione Cariplo, Italy, grant number 2016-0785, and by Ministero dell'Ambiente e della Tutela del Territorio e del Mare, Italy, project DILEMMA – Imaging, Modeling, Monitoring and Design of Earthen Levees.

Data availability

Datasets used in this research will be sent to interested researchers upon request.

References

Apuani, T., Arosio, D., De Finis, E., Stucchi, E., Zanzi, L., Ribolini, A., 2012. Preliminary seismic survey on the unstable slope of Madesimo (northern Italy). In: Proceedings SAGEEP 2012. March 25-29, Tucson, USA.

Archie, G.E., 1942. The electrical resistivity log as an aid in determining some reservoir characteristics. Petr Transact AIME 146, 54–62.

Arosio, D., Boccolari, M., Longoni, L., Papini, M., Zanzi, L., 2017a. Classification of microseismic activity in an unstable rock cliff. In: Mikoš, M., Arbanas, Ž., Yin, Y., Sassa, K. (Eds.), Advancing Culture of Living with Landslides, WLF 2017, vol. 3. Springer, Cham, pp. 123–130. https://doi.org/10.1007/978-3-319-53487-9_13.

Arosio, D., Corsini, A., Giusti, R., Zanzi, L., 2017b. Seismic noise measurements on unstable rock blocks: the case of Bismantova rock cliff. In: Mikoš, M., Arbanas, Ž., Yin, Y., Sassa, K. (Eds.), Advancing Culture of Living with Landslides, WLF 2017, vol. 3. Springer, Cham, pp. 325–332. https://doi.org/10.1007/978-3-319-53487-9_37.

Arosio, D., Hojat, A., Ivanov, V.I., Loke, M.H., Longoni, L., Papini, M., Tresoldi, G., Zanzi, L., 2018a. A laboratory experience to assess the 3D effects on 2D ERT monitoring of river levees. In: 24th European Meeting of Environmental and Engineering Geophysics, Porto. https://doi.org/10.3997/2214-4609.201802628.

Arosio, D., Longoni, L., Mazza, F., Papini, M., Zanzi, L., 2013. Freeze-thaw cycle and rockfall monitoring. In: Margottini, C., Canuti, P., Sassa, K. (Eds.), Landslide Science and Practice: Early Warning, Instrumentation and Monitoring, vol. 2. Springer, Berlin, pp. 385–390. https://doi.org/10.1007/978-3-642-31445-2.

Arosio, D., Longoni, L., Papini, M., Boccolari, M., Zanzi, L., 2018b. Analysis of microseismic signals collected on an unstable rock face in the Italian Prealps. Geophys. J. Int. 213, 475–488. https://doi.org/10.1093/gji/ggy010.

Arosio, D., Longoni, L., Papini, M., Zanzi, L., 2015a. Analysis of microseismic activity within unstable rock slopes. In: Scaioni, M. (Ed.), Modern Technologies for Landslide Monitoring and Prediction, Springer Natural Hazards. Springer, Berlin, pp. 141–154. https://doi.org/10.1007/978-3-662-45931-7.

Arosio, D., Munda, S., Tresoldi, G., Papini, M., Longoni, L., Zanzi, L., 2017. A customized resistivity system for monitoring saturation and seepage in earthen levees: installation and validation. Open Geosci. 9, 457–467. https://doi.org/10.1515/geo-2017-0035.

Arosio, D., Zanzi, L., Longoni, L., Papini, M., 2015b. Microseismic monitoring of an unstable rock face – preliminary signal classification. In: Near Surface Geoscience 2015. September 6-10, Torino.

Baroň, I., Supper, R., 2013. Application and reliability of techniques for landslide site investigation, monitoring and early warning – outcomes from a questionnaire study. Nat. Hazards Earth Syst. Sci. 13, 3157–3168.

Carpentier, S., Konz, M., Fischer, R., Anagnostopoulos, G., Meusburger, K., Schoeck, K., 2012. Geophysical imaging of shallow subsurface topography and its implication for shallow landslide susceptibility in the Urseren Valley, Switzerland. J. Appl. Geophys. 83, 46–56.

Chambers, J.E., Gunn, D.A., Wilkinson, P.B., Meldrum, P.I., Haslam, E., Holyoake, S., Kirkham, M., Kuras, O., Merritt, A., Wragg, J., 2014. 4D electrical resistivity tomography monitoring of soil moisture dynamics in an operational railway embankment. Near Surf. Geophys. 12, 61–72. https://doi.org/10.3997/1873-0604.2013002.

Chambers, J.E., Meldrum, P.I., Gunn, D.A., Wilkinson, P.B., Kuras, O., Weller, A.L., Ogilvy, R.D., 2009. Hydrogeophysical monitoring of landslide processes using automated time-lapse electrical resistivity tomography (ALERT). In: 15th European Meeting of Environmental and Engineering Geophysics.

Crawford, M.M., Bryson, L.S., 2017. Assessment of active landslides using field electrical measurements. Eng. Geol. 233, 146–159.

Crawford, M.M., Bryson, L.S., Woolery, E.W., Wang, Z., 2018. Using 2-D electrical resistivity imaging for joint geophysical and geotechnical characterization of shallow landslides. J. Appl. Geophys. 157, 37–46.

Crawford, M.M., Bryson, L.S., Woolery, E.W., Wang, Z., 2019. Long-term landslide monitoring using soil-water relationships and electrical data to estimate suction stress. Eng. Geol. 251, 146–157.

Cubbage, B., Noonan, G.E., Rucker, D.F., 2017. A modified Wenner array for efficient use of eight-channel resistivity meters. Pure Appl. Geophys. 174, 2705–2718. https://doi.org/10.1007/s00024-017-1535-9.

Dahlin, T., Leroux, V., Larsson, R., Rankka, K., 2005. Resistivity Imaging for Mapping of Quick Clays for Landslide Risk Assessment. Near Surface 2005 (Palermo, Italy).

Dahlin, T., Löfroth, H., Schälin, D., Suer, P., 2013. Mapping of quick clay using geoelectrical imaging and CPTU-resistivity. Near Surf. Geophys. 11, 659–670. https://doi.org/10.3997/1873-0604.2013044.

Dahlin, T., Zhou, B., 2004. A numerical comparison of 2D resistivity imaging with 10 electrode arrays. Geophys. Prospect. 52, 379–398.

Gance, J., Malet, J.P., Supper, R., Sailhac, P., Ottowitz, D., Jochumb, B., 2016. Permanent electrical resistivity measurements for monitoring water circulation in clayey landslides. J. Appl. Geophys. 126, 98–115.

Godio, A., Strobbia, C., De Bacco, G., 2006. Geophysical characterisation of a rockslide in alpine region. Eng. Geol. 83, 273–286.

Grandjean, G., Gourry, J.C., Sanchez, O., Bitri, A., Garambois, S., 2011. Structural study of the Ballandaz landslide (French Alps) using geophysical imagery. J. Appl. Geophys. 75, 531–542.
Heincke, B., Günther, T., Dalsegg, E., Rønning, J.S., Ganerød, J.V., Elvebakk, H., 2010. Combined three-dimensional electric and seismic tomography study on the Åknes rockslide in western Norway. J. Appl. Geophys. 70, 292–306, 2010.
Hojat, A., Arosio, D., Di Luch, I., Ferrario, M., Ivov Ivanov, V., Longoni, L., Madaschi, A., Papini, M., Tresoldi, G., Zanzi, L., 2019a. Testing ERT and fiber optic techniques at the laboratory scale to monitor river levees. In: 25th European Meeting of Environmental and Engineering Geophysics. https://doi.org/10.3997/2214-4609.201902440. The Hague, Netherlands.
Hojat, A., Arosio, D., Loke, M.H., Longoni, L., Papini, M., Tresoldi, G., Zanzi, L., 2019b. Assessment of 3D geometry effects on 2D ERT data of a permanent monitoring system along a river embankment. In: EAGE-GSM 2nd Asia Pacific Meeting on Near Surface Geoscience & Engineering. https://doi.org/10.3997/2214-4609.201900427. Kuala Lumpur, Malaysia.
Hojat, A., Arosio, D., Longoni, L., Papini, M., Tresoldi, G., Zanzi, L., 2019c. Installation and validation of a customized resistivity system for permanent monitoring of a river embankment. In: EAGE-GSM 2nd Asia Pacific Meeting on Near Surface Geoscience & Engineering. Kuala Lumpur, Malaysia. https://doi.org/10.3997/2214-4609.201900421. http://www.iris-instruments.com/. (Accessed 20 November 2018).
Hu, Z., Shan, W., 2016. Landslide investigations in the northwest section of the lesser Khingan range in China using combined HDR and GPR methods. Bull. Eng. Geol. Environ. 75, 591–603.
Iverson, R.M., 2015. Scaling and design of landslide and debris-flow experiments. Geomorphology 244, 9–20.
Kirschbaum, D., Stanley, T., Zhou, Y., 2015. Spatial and temporal analysis of a global landslide catalog. Geomorphology 249, 4–15.
Kuras, O., Pritchard, J.D., Meldrum, P.I., Chambers, J.E., Wilkinson, P.B., Ogilvy, R.D., Wealthall, G.P., 2009. Monitoring hydraulic processes with automated time-lapse electrical resistivity tomography (ALERT). Geoscience 341, 868–885.
Lapenna, V., Lorenzo, P., Perrone, A., Piscitelli, S., Rizzo, E., Sdao, F., 2005. 2D electrical resistivity imaging of some complex landslides in Lucanian Apennine chain, southern Italy. Geophysics 70 (3). https://doi.org/10.1190/1.1926571.
Loke, M.H., 2014. RES3DMODx64 Ver. 3.04: 3-D Resistivity and IP Forward Modeling Using the Finite-Difference and Finite-Element Methods. Geotomosoft Solutions.
Loke, M.H., 2016. RES2DMOD Ver. 3.03: Rapid 2D Resistivity and I.P. Forward Modeling Using the Finite-Difference and Finite-Element Methods. Geotomosoft Solutions.
Loke, M.H., 2018. Rapid 2-D Resistivity and IP inversion using the least-squares method. www.geotomosoft.com. (Accessed 14 August 2018).
Loke, M.H., Acworth, I., Dahlin, T., 2003. A comparison of smooth and blocky inversion methods in 2D electrical imaging surveys. Explor. Geophys. 34, 182–187.
Longoni, L., Arosio, D., Scaioni, M., Papini, M., Zanzi, L., Roncella, R., Brambilla, D., 2012. Surface and subsurface non-invasive investigations to improve the characterization of a fractured rock mass. J. Geophys. Eng. 9 (5), 461–472. https://doi.org/10.1088/1742-2132/9/5/461.
Longoni, L., Papini, M., Arosio, D., Zanzi, L., Brambilla, D., 2014. A new geological model for Spriana landslide. Bull. Eng. Geol. Environ. 73, 959–970.
Lundberg, E., Malehmir, A., Juhlin, C., Bastani, M., Andersson, M., 2014. High-resolution 3D reflection seismic investigation over a quick-clay landslide scar in southwest Sweden. Geophysics 79 (2), B97–B107.
Lundström, K., Larsson, R., Dahlin, T., 2009. Mapping of quick clay formations using geotechnical and geophysical methods. Landslides 6 (1), 1–15.
Menziani, M., Rivasi, M.R., Pugnaghi, S., Santangelo, R., Vincenzi, S., 1996. Soil volumetric water content measurements using TDR technique. Ann. Geofisc. XXXIX (1), 91–96.
Merritt, A.J., Chambers, J.E., Murphy, W., Wilkinson, P.B., West, L.J., Gunn, D.A., Meldrum, P.I., Kirkham, M., Dixon, N., 2014. 3D ground model development for an active landslide in Lias mudrocks using geophysical, remote sensing and geotechnical methods. Landslides 11 (4), 537–550.
Michlmayr, G., Chalari, A., Clarke, A., Or, D., 2017. Fiber-optic high-resolution acoustic emission (AE) monitoring of slope failure. Landslides 14 (3), 1139–1146.
Michlmayr, G., Cohen, D., Or, D., 2013. Shear-induced force fluctuations and acoustic emissions in granular material. J. Geophys. Res. 118 (12), 6086–6098.
Milledge, D.G., Griffiths, D.V., Lane, S.N., Warburton, J., 2012. Limits on the validity of infinite length assumptions for modelling shallow landslides. Earth Surf. Process. Landforms 37 (11), 1158–1166.
Montrasio, L., Valentino, R., 2008. A model for triggering mechanisms of shallow landslides. Nat Hazards Earth Sys 8 (5), 1149–1159.
Montrasio, L., Valentino, R., 2016. Modelling rainfall-induced shallow landslides at different scales using SLIP - Part I. Procedia Eng 158, 476–481.
Mooney, H.M., 1980. Handbook of Engineering Geophysics; Electrical Resistivity. Binson Instrumentation.
Olivares, L., Damiano, E., Greco, R., Zeni, L., Picarelli, L., Minardo, A., Guida, A., Bernini, R., 2009. An instrumented flume to investigate the mechanics of rainfall-induced landslides in unsaturated granular soils. Geotech. Test J. 32 (2), 108–118. https://doi.org/10.1520/GTJ101366.
Perrone, A., Lapenna, V., Piscitelli, S., 2014. Electrical resistivity tomography technique for landslide investigation: a review. Earth Sci. Rev. 135, 65–82.
Polemio, M., Petrucci, O., 2000. Rainfall as a landslide triggering factor: an overview of recent international research. In: The 8th International Symposium on Landslides in Cardiff.
Reid, M.E., LaHusen, R.G., Baum, R.L., Kean, J.W., Schulz, W.H., Highland, L.M., 2012. Fact Sheet 2012-3008. In: Real-time Monitoring of Landslides. USGS.
Ross, B., 2017. Rise to the Occasion; Lessons from the Bingham Canyon Manefay Slide. SME, p. 244.
Scaioni, M., Crippa, J., Longoni, L., Papini, M., Zanzi, L., 2017. Image-based reconstruction and analysis of dynamic scenes in a landslide simulation facility. ISPRS Ann. Photogramm. Remote Sens. Spatial Inf. Sci. IV (5/W1), 63–70. https://doi.org/10.5194/isprs-annals-IV-5-W1-63-2017.
Scaioni, M., Crippa, J., Yordanov, V., Longoni, L., Ivanov, V.I., Papini, M., 2018. Some tools to support teaching photogrammetry for slope stability assessment and monitoring. International Archives of the Photogrammetry. ISPRS Ann. Photogramm. Remote Sens. Spatial Inf. Sci. 42 (3W4), 453–460.
Schenato, L., Palmieri, L., Camporese, M., Bersan, S., Cola, S., Pasuto, A., Galtarossa, A., Salandin, P., Simonini, P., 2017. Distributed optical fibre sensing for early detection of shallow landslides triggering. Sci. Rep. 7, 14686 https://doi.org/10.1038/s41598-017-12610-1.
Sjödahl, P., Dahlin, T., Johansson, S., Loke, M.H., 2008. Resistivity monitoring for leakage and internal erosion detection at Hällby embankment dam. J. Appl. Geophys. 65 (3–4), 155–164.
Supper, R., Ottowitz, D., Jochum, B., Kim, J.H., Romer, A., Baron, I., Pfeiler, S., Lovisolo, M., Gruber, S., Vecchiotti, F., 2014. Geoelectrical monitoring: an innovative method to supplement landslide surveillance and early warning. Near Surf. Geophys. 12 (1), 133–150. https://doi.org/10.3997/1873-0604.2013060.
Supper, R., Römer, A., Jochum, B., Bieber, G., Jaritz, W., 2008. A complex geo-scientific strategy for landslide hazard mitigation from airborne mapping to ground monitoring. Adv. Geosci. 14, 195–200.
Telford, W.M., Geldart, L.P., Sheriff, R.E., 1990. Applied Geophysics. Cambridge University Press, p. 770.
Topp, G.C., Davis, J.L., Bailey, W.G., Zebchuk, W.D., 1984. The measurement of soil water content using a portable TDR hand probe. Can. J. Soil Sci. 64, 313–321.
Tresoldi, G., Arosio, D., Hojat, A., Longoni, L., Papini, M., Zanzi, L., 2018. Tech-Levee-Watch: experimenting an integrated geophysical system for stability assessment of levees. Rendiconti Online della Società Geologica Italiana 46, 38–43. https://doi.org/10.3301/ROL.2018.49.
Tresoldi, G., Arosio, D., Hojat, A., Longoni, L., Papini, M., Zanzi, L., 2019. Long-term hydrogeophysical monitoring of the internal conditions of river levees. Eng. Geol. 259, 105139 https://doi.org/10.1016/j.enggeo.2019.05.016.
Wang, S., Malehmir, A., Bastani, M., 2016. Geophysical characterization of areas prone to quick-clay landslides using radio-magnetotelluric and seismic methods. Tectonophysics 677–678, 248–260.
Whiteley, J., Chambers, J.E., Uhlemann, S., 2017. Integrated monitoring of an active landslide in lias group mudrocks, north yorkshire, UK. In: Hoyer, S. (Ed.), GEL-MON 2017: 4th International Workshop on Geoelectrical Monitoring: Book of Abstracts, p. 27.
Wieczorek, G.F., 1996. Landslide triggering mechanisms. In: Turner, A.K., Schuster, R.L. (Eds.), Landslides: Investigation and Mitigation. National Research Council Transportation Research Board, vol. 247. Special Report, pp. 76–90.
Winter, M.G., Shearer, B., Palmer, D., Peeling, D., Harmer, C., Sharpe, J., 2016. The economic impact of landslides and floods on the road network. Procedia Engineering 143, 1425–1434.